Crystallographic analysis of the Dome Fuji ice core

Nobuhiko Azuma*, Yun Wang*, Yasuo Yoshida*, Hideki Narita**, Takeo Hondoh**, Hitoshi Shoji*** and Okitsugu Watanabe****

*Nagaoka University of Technology, Nagaoka, Niigata 940-2137, JAPAN
**ILTS, Hokkaido University, N19W8, Sapporo 060-0819, JAPAN
***Kitami Institute of Technology, Koencho 165, Kitami 090-0015, JAPAN
****National Institute of Polar Research, Kaga 1-9-10, Itabashi, Tokyo 173-0003, JAPAN

Abstract: A comprehensive study of ice crystal fabrics and textures on the Dome Fuji ice core shows that 1) nucleation-recrystallization did not occur, 2) the distribution of c-axes gradually changes with depth from a random orientation pattern near the surface to one with a single, sharp maximum in the vertical at 2500 m, 3) the mean crystal size steadily increases with depth except for abrupt decreases near 420, 1800, 2000, 2200, and 2300 m; and 4) the aspect ratio of individual crystals increases with depth until 1500 m. Analysis of the misorientation angle between adjacent crystals indicates that rotation-recrystallization was activated below 1300 m. Also, the clustering of c-axes is weakened at depths containing layers with high impurity concentrations.

1. Introduction

The first comprehensive study of textures and fabrics in deep ice cores was done by Gow and Williamson [1976] using the Byrd ice core. Subsequent crystallographic studies of deep ice cores provided substantial information about the ice flow conditions and the physical properties of ice in ice sheets [Herron and Langway, 1982; Herron et al., 1985; Langway et al., 1988; Lipenkov et al., 1989; Thorsteinsson et al., 1997; Gow et al., 1997]. Gow and Williamson [1976] found that the crystal size increases with depth above 400 m and then keeps constant until the Holocene-Wisconsin boundary near 1200 m. Below this boundary, the crystal size decreases and has more c-axes oriented near the vertical. Crystallographic studies of the Dye3 ice core [Herron et al., 1985; Langway et al., 1988] showed that the crystal size decreases abruptly and the c-axes cluster tightly below the Holocene-Wisconsin boundary at 1786 m. In contrast to the above flank-region sites (Byrd and Dye3), the GRIP core [Thorsteinsson et al., 1997] and GISP2 core [Gow et al., 1997], which are both from Summit, Central Greenland, did not have significant c-axis clustering between the Holocene and Wisconsin ice, although the crystal size decreased abruptly below the Holocene-Wisconsin boundary. Thorsteinsson et al. [1995] studied regions of the Eemian ice where the crystal size changed within several centimeters, and found that the fabric strength was related to crystal size; the fine-grained ice had a strong single maximum whereas the coarse-grained ice

Physics of Ice Core Records
Edited by T. Hondoh
Hokkaido University Press, 2000, Sapporo

had weaker fabrics. In addition, the Dome Fuji core had weaker c-axis clustering in layers with high impurity concentrations [Azuma et al., 1999].

In the following, we first overview complete data sets on textures and fabrics in the Dome Fuji ice core. Then we focus on characteristic features such as rotation-recrystallization, and the relationship between textures and fabrics at low temperatures and strain rates where nucleation(migration)-recrystallization does not occur.

2. General features of textures and fabrics thorough 2500 m

Thin sections 10-cm long, 5-cm wide, and 0.5-mm thick were cut parallel to the core axis in a cold room at −20 °C and prepared using standard methods. In 1996 and 1997, basic sampling and measurements were done at 20-m intervals from 100 to 2250 m; in addition, continuous 1-m sections along the core were measured at ten selected depths between 500 and 1900 m. In 1998 and 1999, basic sampling and measurements were done at 10-m intervals below 1500 m.

We developed an automatic ice fabric analyzer to measure c-axis orientation, crystal size, and crystal shape on these thin sections [Wang and Azuma, 1999; Azuma et al., 1999]. The crystal images were input to a personal computer (PC) by a charge-coupled device (CCD) camera and individual crystals were recognized using image-analysis techniques. The PC can quickly calculate crystal parameters such as size, elongation direction, aspect ratio (length along the long axis to that along the short axis), and c-axis orientations of all individual crystals in view of the CCD camera. The viewing diameter was 3.5 cm; thus three views from the CCD camera covered one 10-cm length.

Images of each crystal taken at ten different polarizing directions were processed with several image filters to accurately distinguish crystal boundaries and 2D crystal shapes on the section plane. When the c-axis orientations between adjacent crystals were so close that differences in their interference colors were too small for the imaging software to detect their boundaries, the proper grain boundaries were drawn manually on the images. Individual crystal areas were calculated then sized by the diameter of the equal area circle. We hereafter call this equivalent diameter the "crystal size". The average crystal size was calculated for each thin section. The c-axis orientations of individual crystals on each thin section were plotted on a Schmidt net. Several statistical parameters to express the c-axis orientation strength and direction were calculated for each thin section. The mean orientation of c-axes (MOC) is defined as the orientation of the vector obtained by summing the c-axis unit vectors for all crystals. This orientation corresponds to a pole of single maximum on the Schmidt net. To quantify the alignment around the mean orientation, we calculated the median inclination of c-axes (MIC) in reference to the MOC, which is defined as the half apex angle of the cone containing half the measured c-axes. The MIC is zero for completely aligned c-axes and is 60 degrees for a uniform distribution of c-axes. The borehole is within 1 degree of vertical until 1800 m and then deviates with depth, reaching a maximum of 4.6 degrees at 2250 m [Dome-F Deep Coring Group, 1998];

therefore, the longitudinal axis of the thin section, being parallel to the core axis, is not geographically vertical. An alternative method to determine the c-axis distribution is to calculate eigenvectors and eigenvalues for each set of c-axis data [Herron and Langway, 1982; Thorsteinsson, 1996]. The eigenvectors are the three orthogonal principal axes of the normalized ellipsoid that best fits the c-axis orientation data. The eigenvalues are the lengths of these axes.

Crystal size and c-axis orientation fabric

Figure 1 shows the fabric diagrams and thin section photographs from the CCD camera at selected depths. The center of each fabric diagram coincides with the core axis and the up-down direction of each photograph coincides with that of the core.

The depth profile of the frequency distribution of the c-axis inclination with respect to the core axis, and a similar profile for the crystal size are in Figures 2(a) and 2(b), respectively. The mean crystal size and the median inclination profiles are presented in Figure 3. (Measurements were not done between the surface and 112 m.) The mean crystal size is nearly constant at 2 mm from 112 to 420 m. Between 420 and 700 m the mean crystal size decreases, and then it steadily increases with depth except for abrupt decreases at depths of around 1800, 2000, 2200, and 2300 m. The maximum value of 10.3 mm is at 2490 m.

As shown in Fig. 1, the c-axis orientation fabrics gradually change with depth from a random orientation pattern near the surface to one with a strong vertical single maximum; a development which is very similar to that observed in the GRIP core [Thorsteinsson et al., 1997]. The median inclination varies from 54 degrees at 112 m to 9 degrees at 2500 m. Throughout all sampling depths, no characteristic fabric patterns such as small girdle, great girdle, and multi-maxima were observed, although there are deviations of c-axes concentration in the frequency distribution profile (Fig. 2(a)) and in the median inclination profile (Fig. 3).

Figure 4 shows three eigenvalues (E_1, E_2, E_3) of the c-axis orientation fabrics. The largest eigenvalue (E_3) indicates the axial concentration of c-axes about the MOC; values close to unity, the maximum value, indicate a preferred orientation. If the c-axes are symmetrically distributed about the preferred orientation, the other two eigenvalues (E_1 and E_2) are equal. However, measured differences between E_1 and E_2 at all depths suggest that the c-axis distributions do not have a perfect circular single maximum, but are elongated horizontally.

The profile of the MOC, the angle between the pole of the single maximum and the core axis, is in Figure 5. The MOC stayed constant at 2±2 degrees until 1900 m; below this depth, the MOC increased to 14 degrees at 2490 m with large fluctuations. According to the borehole inclination data [Dome-F Deep Coring Group, 1998], the borehole deviation from the vertical increases with depth below 1800 m and has a maximum of 4.6 degrees at 2250 m. Although the inclination of the MOC with respect to the vertical can not be known because there is no information about the orientation of the ice core within the borehole, the large deviation of the MOC from the core axis below 2000 m is more than the borehole inclination. Hence, the mean orientation of the c-axes was at least several degrees from the vertical below 2000 m. Below 2000 m, visual

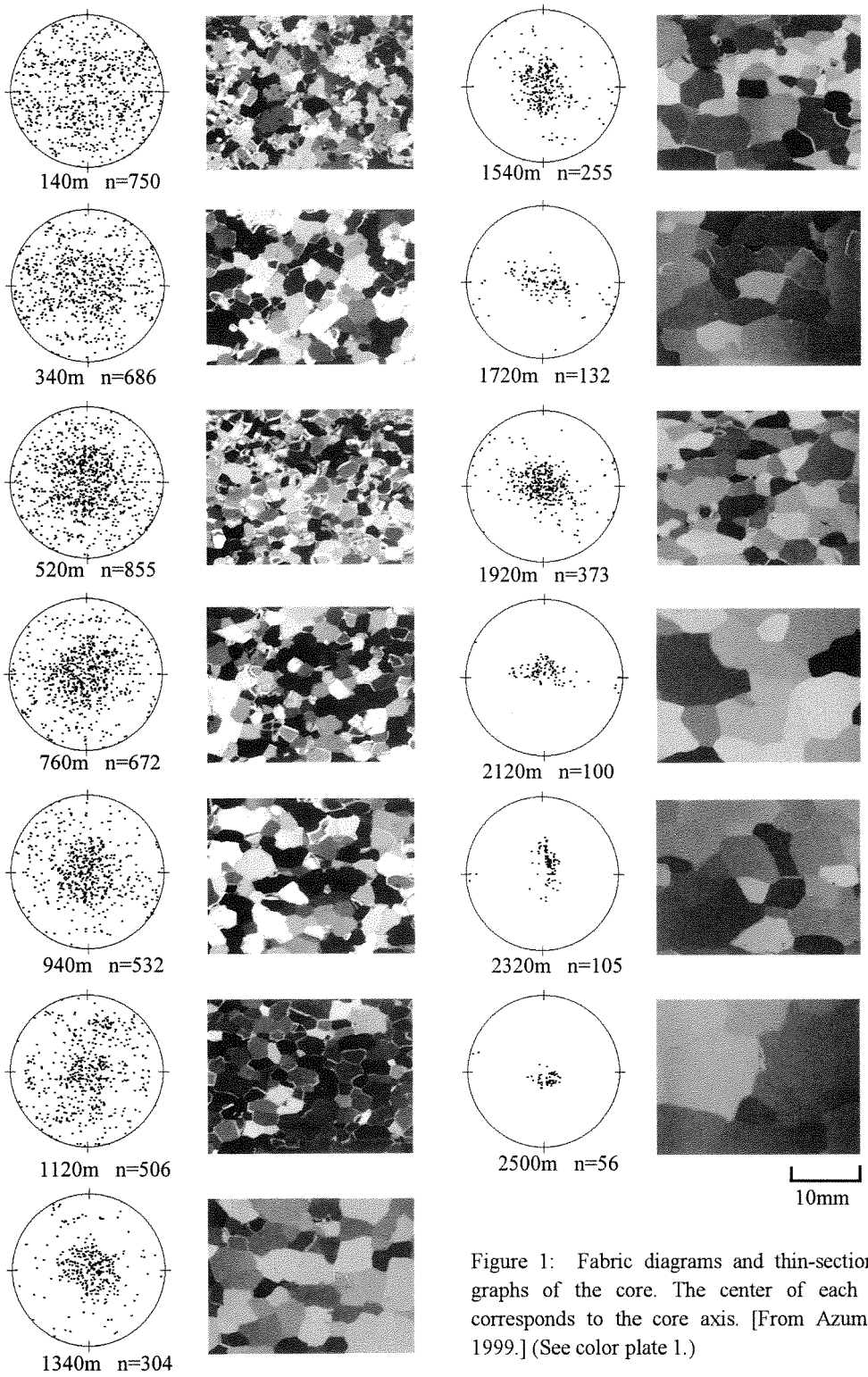

Figure 1: Fabric diagrams and thin-section photographs of the core. The center of each diagram corresponds to the core axis. [From Azuma et al., 1999.] (See color plate 1.)

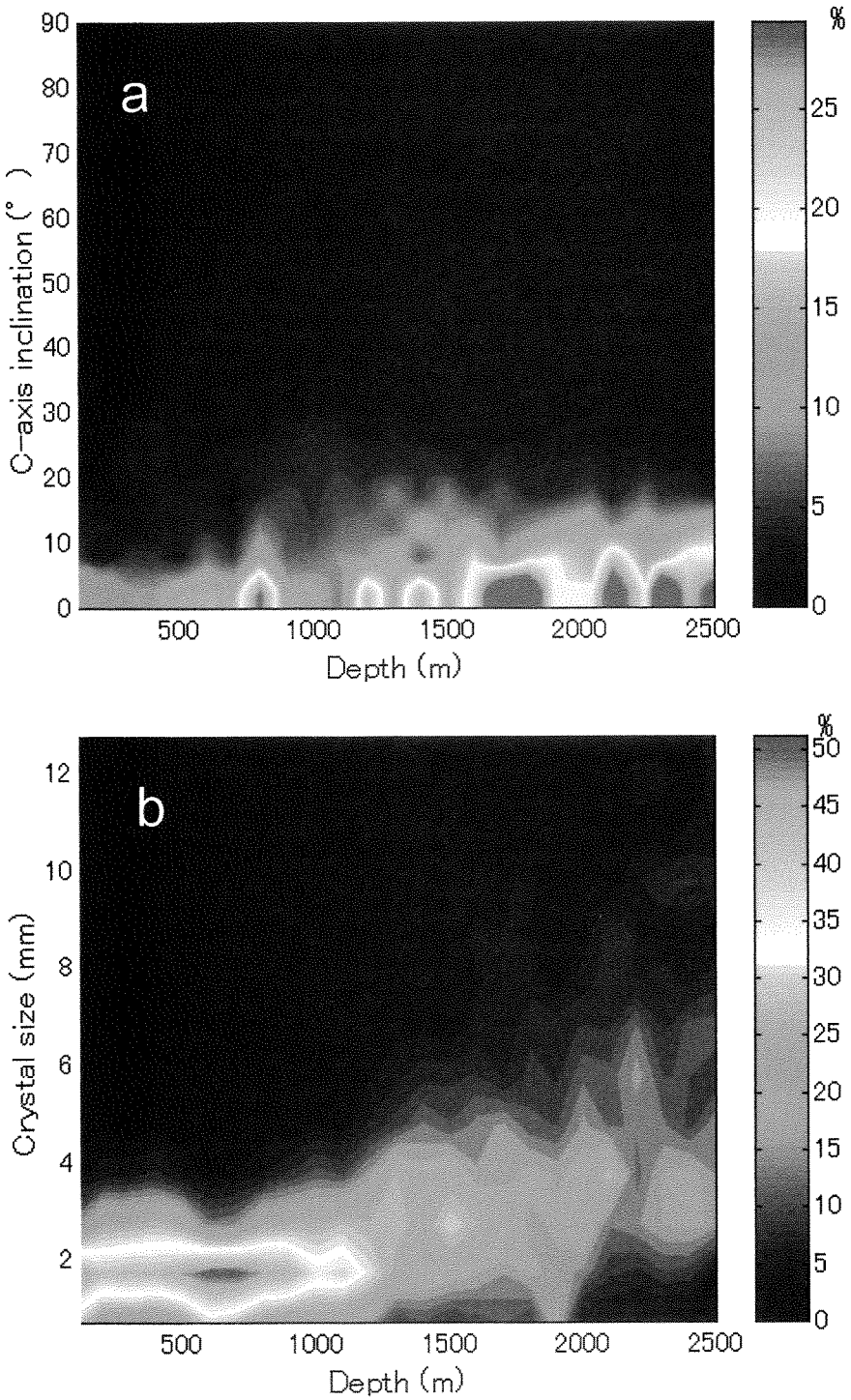

Figure 2: Frequency distributions of (a) c-axis inclination, and (b) crystal size vs. depth. (See color plate 2.)

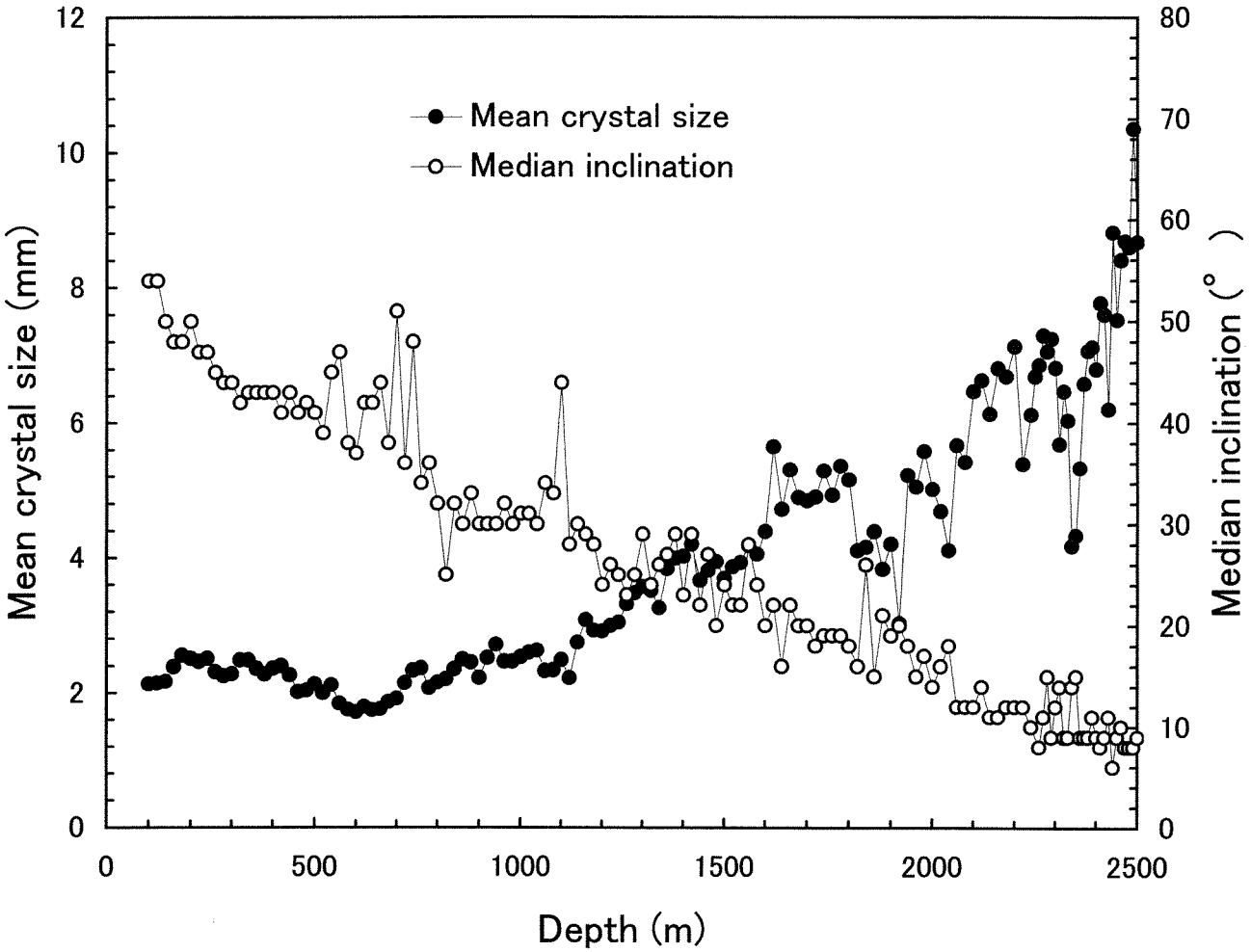

Figure 3: Mean crystal size and median inclination of c-axes. Crystal size means equivalent-area diameter of the two-dimensional crystal sections in the thin-sections. [From Azuma et al., 1999 with changes.]

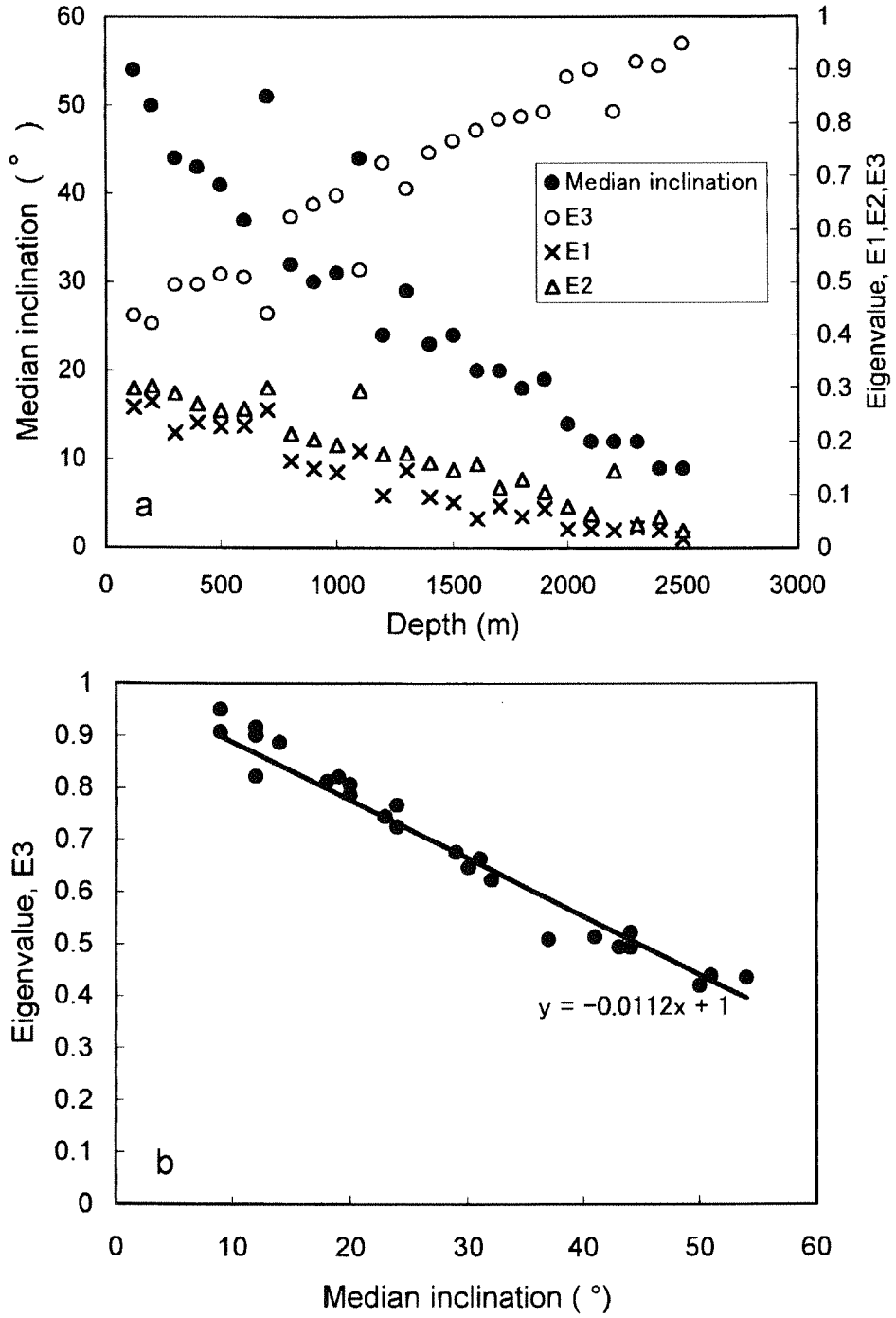

Figure 4: Three eigenvalues (E_1, E_2, E_3) of the c-axis-orientation fabrics. The largest eigenvalue (E_3) indicates the axial concentration of c-axes about the MOC. The maximum value is unity, and high values indicate preferred orientations. If the c-axes orientations are symmetrically distributed on an axis, the other two (E_1 and E_2) are equal.

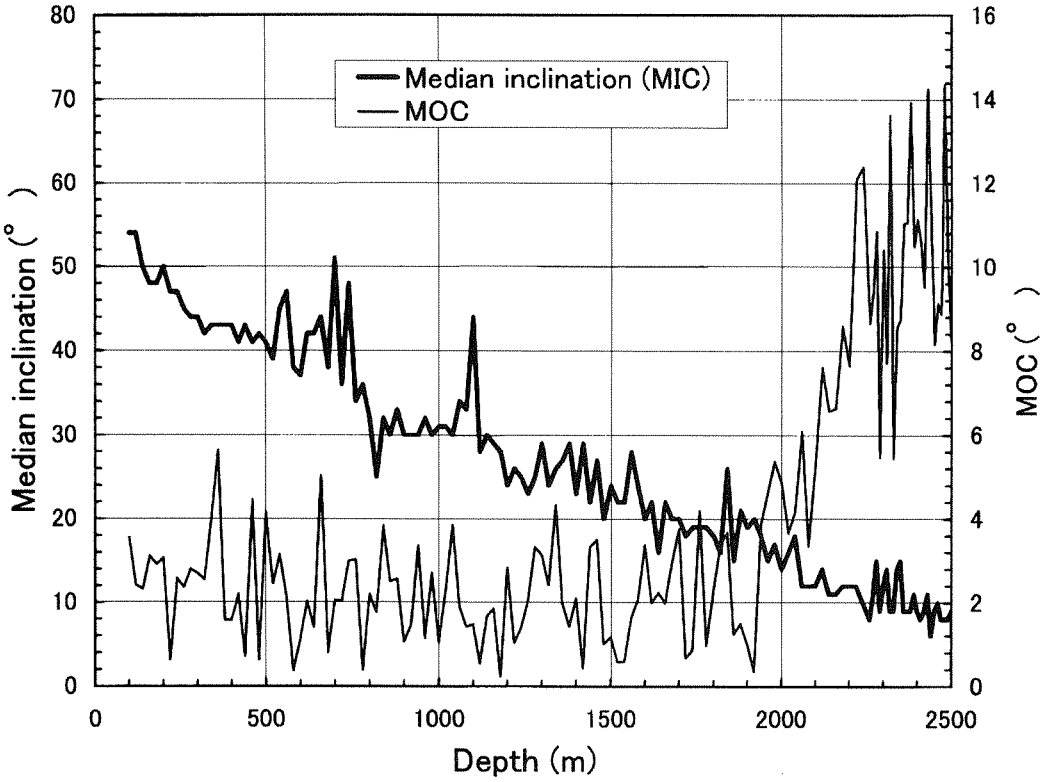

Figure 5: Median inclination (thick line) and mean orientation of c-axes MOC (thin line). The mean orientation of c-axes is defined as the angle between the core axis and the orientation of a vector obtained by the sum of all unit vectors parallel to c-axis. [From Azuma et al., 1999.]

stratigraphy observations found tephra layers and cloudy bands inclined about ten degrees with respect to the normal plane of the core axis. Therefore, it is likely that the layers below 2000 m are inclined with respect to the horizontal due to the influence of bedrock topography.

Crystal shape and its variation with depth

As can be seen in the thin section photographs in Figure 1, crystals in deeper regions are more elongated in the horizontal direction than shallower crystals. Figure 6 shows the frequency distribution of crystal aspect ratio versus depth. (Because we measured each crystal's aspect ratio and elongation direction on a vertical thin section, these indicate 2-dimensional, not 3-dimensional characteristics.) It was rare to find crystals with an aspect ratio larger than two. This result suggests that the crystals are subdivided by sub-boundary formation due to a pile-up of dislocations during crystal deformation, and this prevents crystals from elongating more than twice the short axis length. This phenomenon is observed in the Vostok cores [Lipenkov et al., 1989], the Byrd cores [Alley et al., 1995], the GRIP cores [Thorsteinsson et al., 1996], and the GISP II cores [Alley et al.,

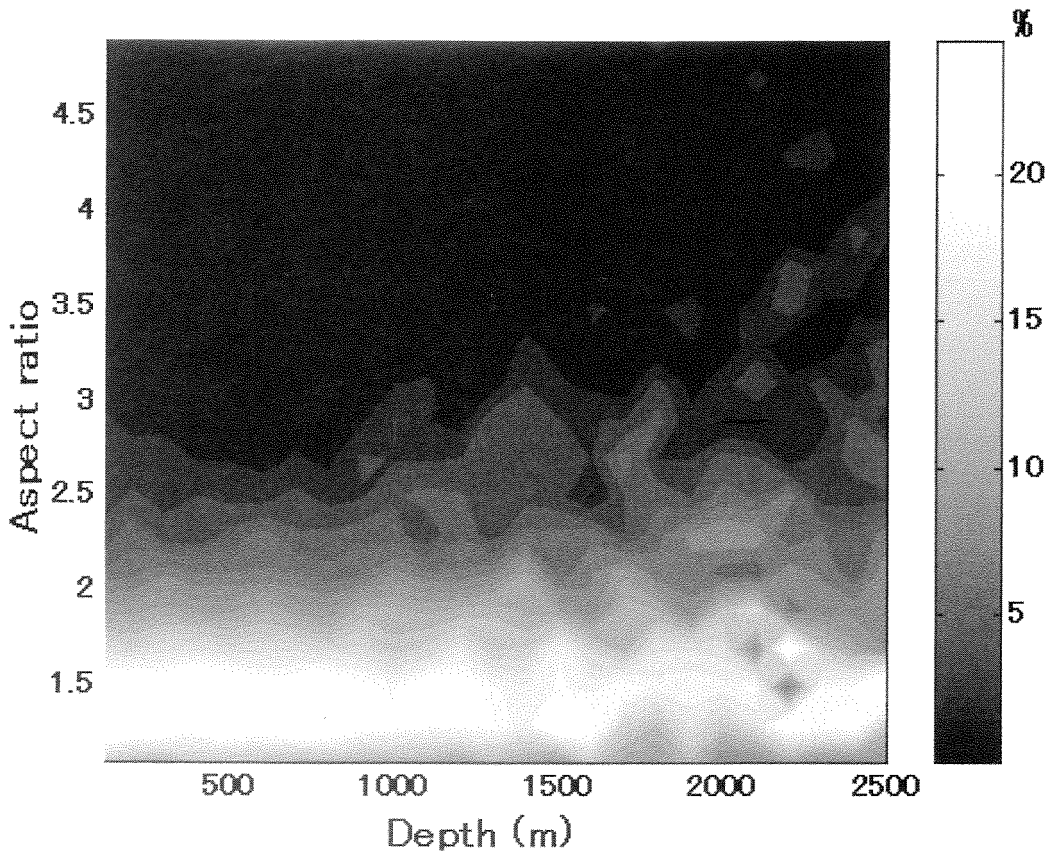

Figure 6: Frequency distribution of crystal aspect ratio vs. depth. (See color plate 3.)

1996]; it is called "rotation-recrystallization" [Duval, in this volume].

Crystal shapes were not equi-axial, but were elongated at shallow depths and their elongated directions varied with depth. Figure 7 shows a circular histogram of the crystal elongation direction. Directions 0 and 180 degrees are along the core axis. At the shallow depth of 120 m, the long axes of crystals orient in various directions; however, the number of crystals elongated horizontally increases with depth. A typical example is the diagram for 2340 m in Figure 7. These features are more clearly seen in Fig. 8, which shows the frequency distribution of crystal elongation directions versus depth.

Profiles of the mean aspect ratio (MAR) of crystals and the mean crystal elongation direction (MCED) are presented by the thick and the thin line, respectively in Figure 9. The MAR is nearly constant at 1.7 for depths down to 800 m and then it increases with depth until 1500 m. Between this depth and 2500 m, it fluctuates about 1.9. The MCED indicates the mean angle between the crystal elongation direction and the core axis. It would be 90 degrees if all crystals elongate horizontally. The MCED increases with depth for the first 1000 m, and then it keeps constant with large

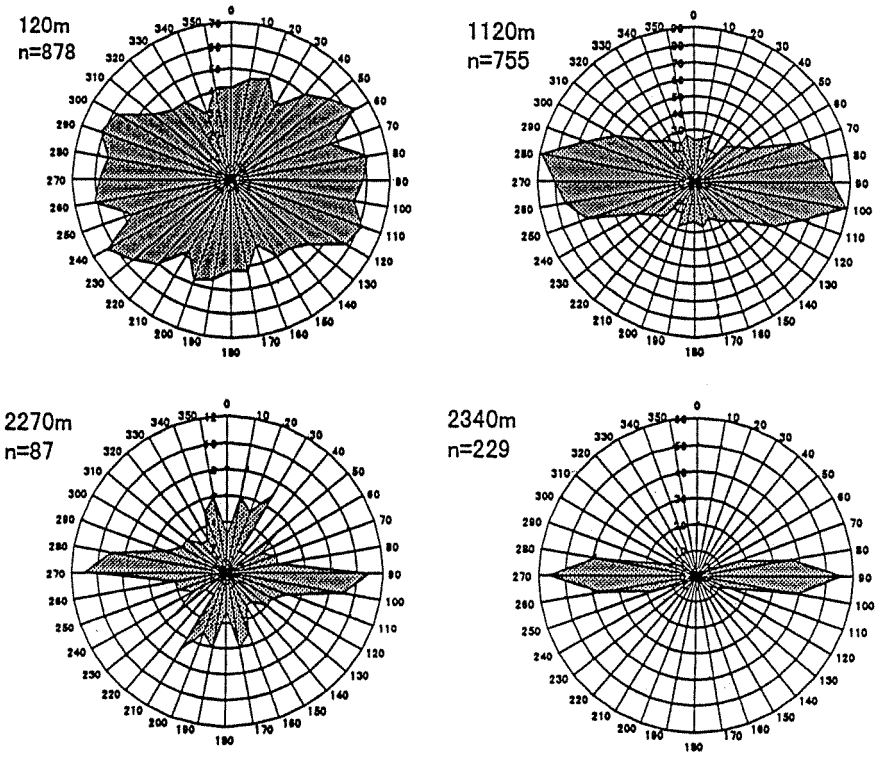

Figure 7: Circular histogram of the crystal elongation direction. Angles 0 and 180 degrees are parallel to the core axis. [From Azuma et al., 1999.]

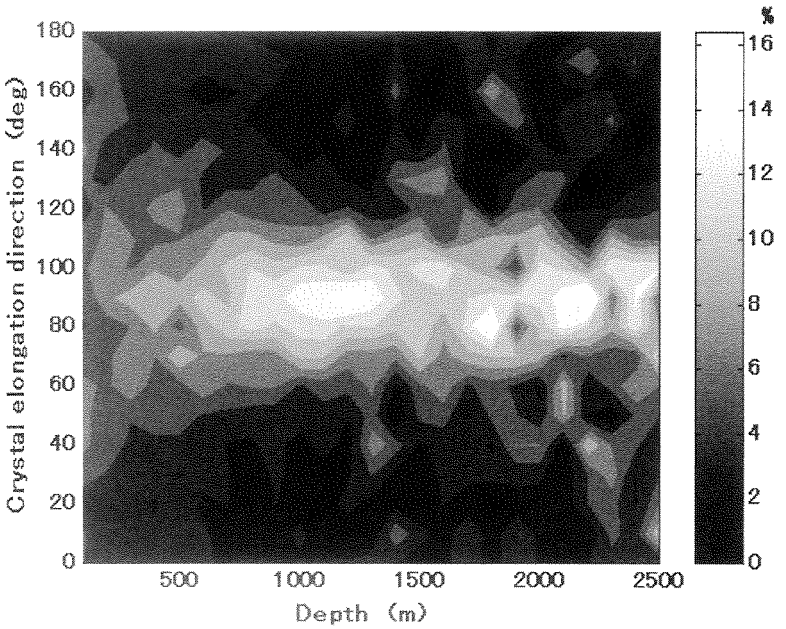

Figure 8: Frequency distribution of crystal elongation direction vs. depth. (See color plate 4.)

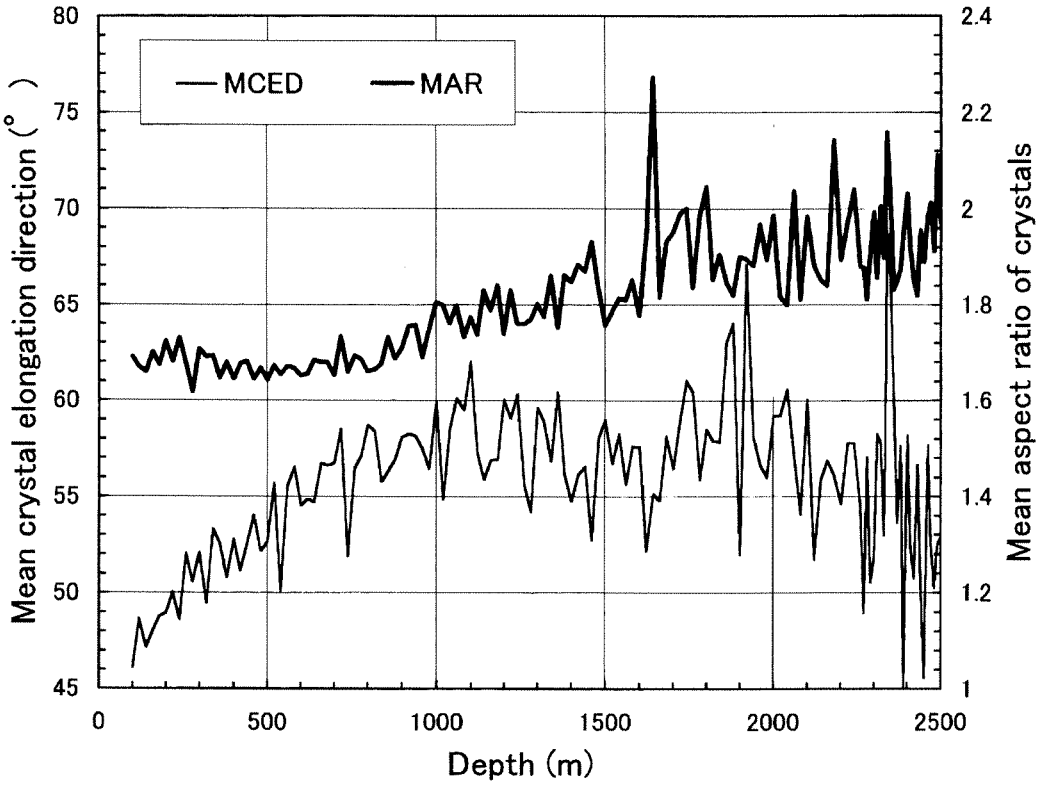

Figure 9: Mean crystal-elongation direction MCED (thin line) and mean crystal aspect ratio MAR (thick line). The mean crystal-elongation direction is the mean angle between the crystal-elongation axis and the core axis. [From Azuma et al., 1999.]

fluctuations until 2000 m. Below this depth it decreases, but with large fluctuations. Because the MCED is between 50° and 60° at most depths, a large fraction of the crystals elongate horizontally; however, Fig. 8 shows that a considerable number of crystals elongate in other directions.

3. Interpreting the textures and fabrics

As described in the above section, rotation-recrystallization likely occurs beneath Dome Fuji. Because rotation-recrystallization is caused by segmentation due to the formation of sub-boundaries in deformed crystals, misorientations between the newly-divided grains should be small. As demonstrated by Alley et al. [1995], this can be examined by measuring the frequency that adjacent-grain pairs have a low c-axis-misorientation angle. Figures 10(a) and 10(b) show the frequency distribution of the c-axis-misorientation angle between adjacent grains and that of random combination of two grains, respectively. This data included all thin sections of the Dome Fuji core. In general, the frequency of low misorientation angle increases with depth in both diagrams because the c-axis for all crystals rotate toward the vertical with depth. However,

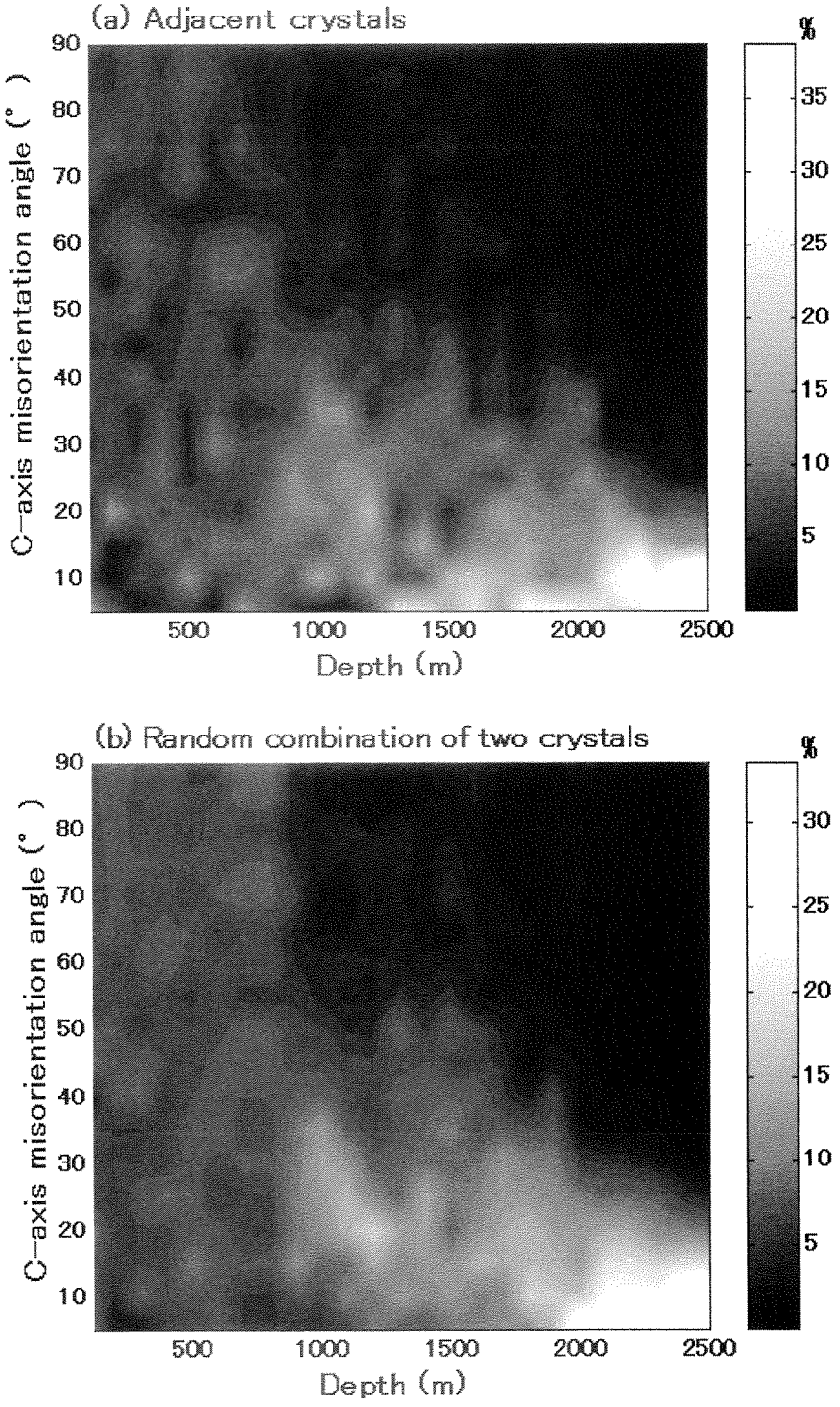

Figure 10: Frequency distributions of (a) the angle between c-axes of adjacent grains (misorientation angle), and (b) the misorientation angle of two randomly-chosen grains. (See color plate 5.)

high frequencies of low misorientation angles less than ten degrees occurs between 1300 and 2000 m for adjacent crystals as compared with the random pairing of crystals. This suggests that rotation-recrystallization is activated below 1300 m at Dome Fuji. Further evidence of this is in the thin sections of Fig. 11. The straight line indicated by an arrow is a small angle boundary. Figure 10 (a) also shows that high misorientation angles between adjacent grains did not occur at these depths. This means that nucleation(migration)-recrystallization does not occur in the ice sheet above 2500 m at Dome Fuji.

Figure 12 shows that the median inclination of c-axes is larger near depths of 500 to 700 m, 1100 m, 1800 to 1900 m, and 2300 m; i.e., the clustering of c-axes about the vertical is weakened at these depths. These depths are also characterized as having high-impurity-concentration layers and are depths at which crystal size decreases.

According to the many observations of textures and fabrics of polar ice cores [Thorsteinsson, 1996, Langway et al., 1988, Koerner and Fisher, 1979], high-impurity ice produces smaller crystal sizes and stronger c-axis clustering. The latter is contrary to the Dome Fuji data.

Although we cannot explain this disagreement, we suggest the following possibility.

At low temperatures and at low deviatoric stress, the ratio of diffusion creep

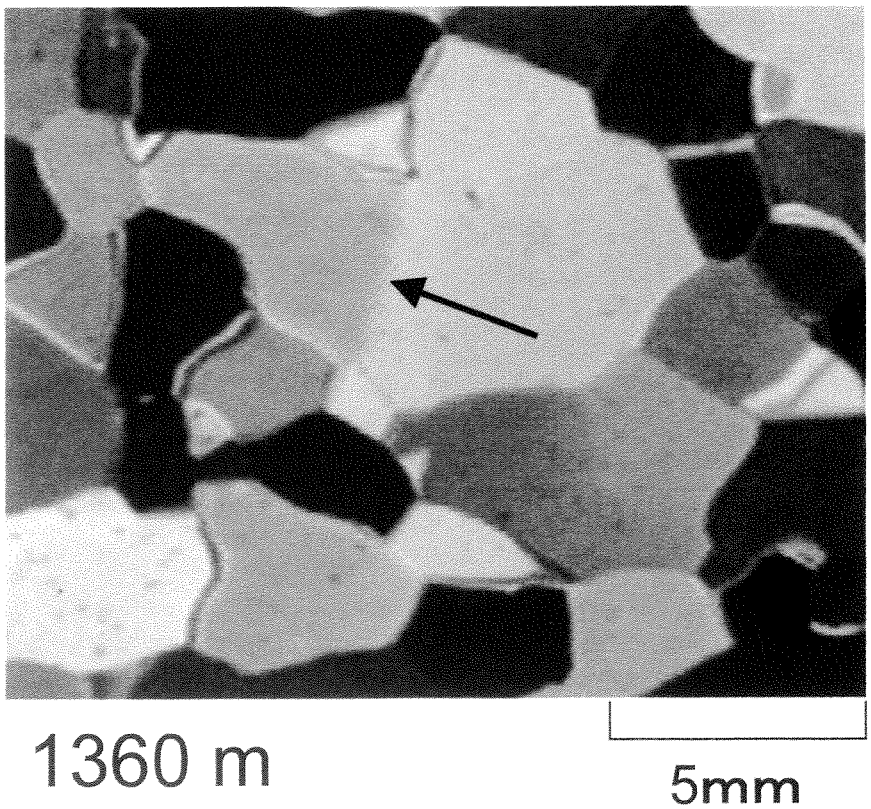

Figure 11: Sub-boundary in a crystal from the core.

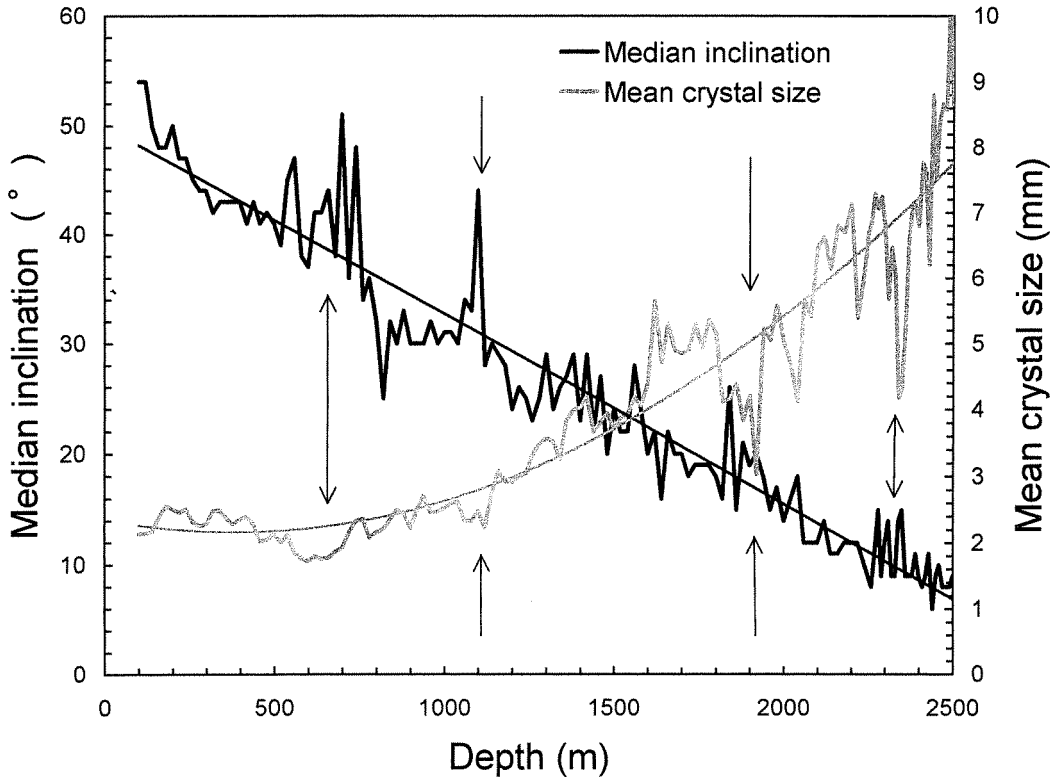

Figure 12: Correlation between the median inclination angle and the mean crystal size.

to dislocation glide becomes significant and increases with decreasing grain size. Figure 13 shows the ratio of deformation rate due to dislocation glide to the total deformation rate (dislocation + diffusion), which were calculated using the deformation mechanism map [Goodman et al., 1977, Shoji and Higashi, 1978]. The calculations were done at four constant total-strain rates ($5x10^{-6}a^{-1}$, $1x10^{-5}a^{-1}$, $1.5x10^{-5}a^{-1}$ and $2x10^{-5}$ a^{-1}) that reasonably describe the ice sheet vertical strain rate at Dome Fuji. The crystal size-profile for the Dome Fuji core is also plotted in each diagram; it assumes the present ice-sheet-temperature profile [Johnsen, personal communication]. The diagrams show that the diffusion creep rate in high impurity layers (620, 1920,and 2340 m) reaches 30 % to 50 % of the total creep rate. This decreased role of dislocation glide in the total deformation could slow down the c-axis clustering because diffusion creep does not lead to clustering.

Figure 14 shows the crystal size variation versus the oxygen isotope ratio [Watanabe et al., 1999]. Although the crystal data were at less precise sampling intervals than the isotope data, the highs and lows of the crystal size profile correlate with the isotope variation. This agrees with GRIP core results [Thorsteinsson et al., 1997] and Vostok core results [Lipenkov et al., 1989]. Thorsteinsson [1996] analyzed correlations between crystal size, isotope

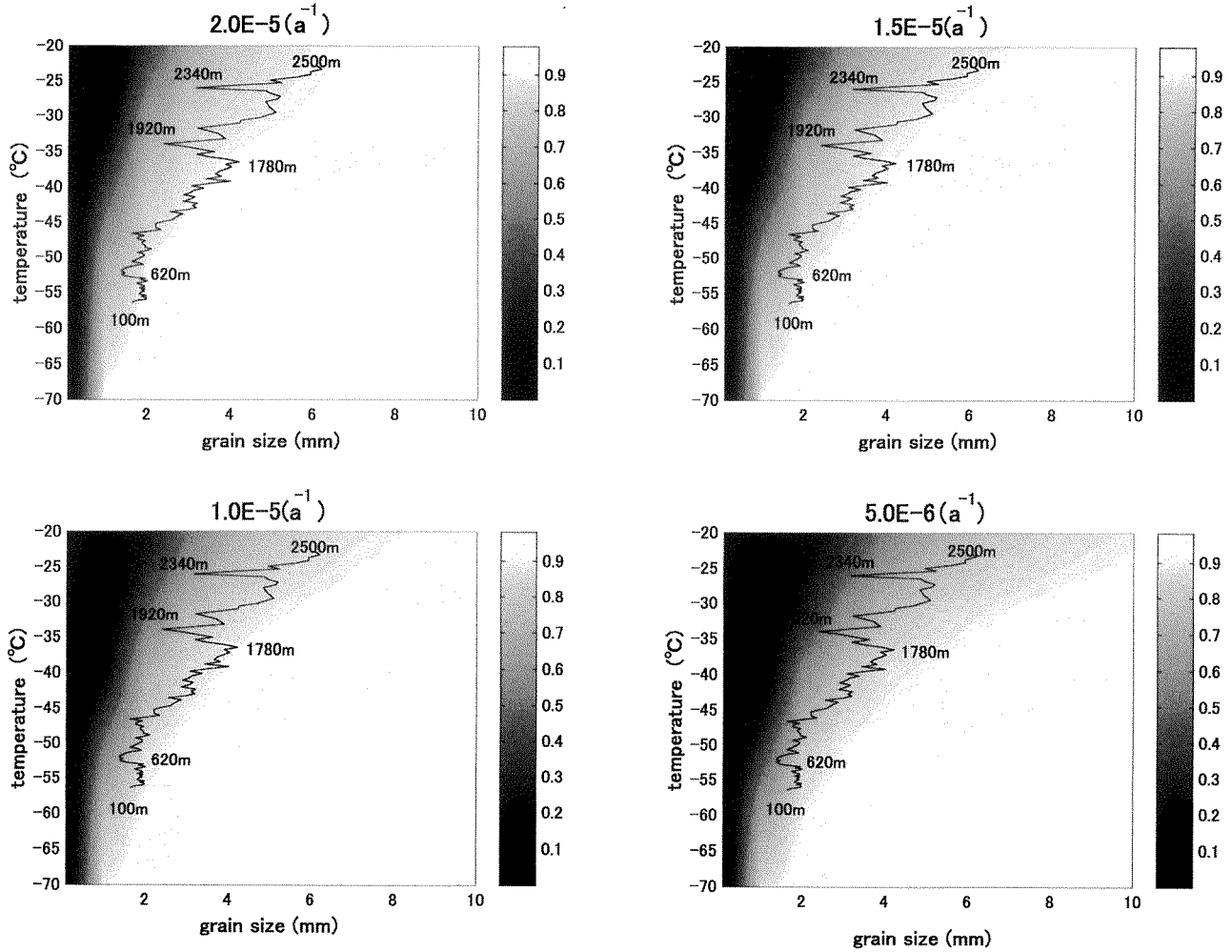

Figure 13: Ratio of deformation rate due to the dislocation glide to the total deformation rate (dislocation + diffusion) in the Dome Fuji ice sheet, which was calculated using the deformation mechanism map [Goodman et al., 1977; Shoji and Higashi, 1978]. (See color plate 6.)

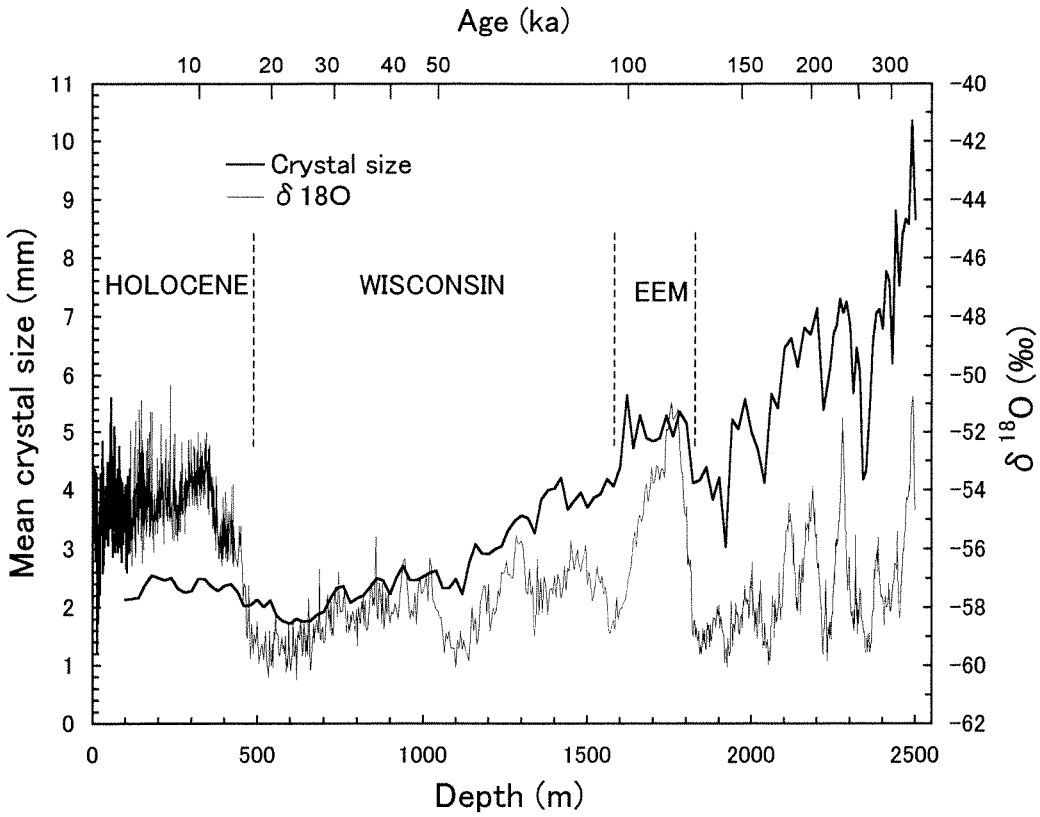

Figure 14: Crystal size variation and the oxygen isotope ratio. [From Azuma et al., 1999.]

ratio, and impurity concentration in the GRIP core; high concentrations of impurities slowed grain growth when calcium concentrations exceeded 12 ppb, chloride concentrations exceeded 20 ppb, or the dust content rose above 0.5 mg/l. In the Dome F core, the impurity concentrations at depths where crystal size decreased exceeded 40 ppb for Ca^{2+}, and 100 ppb for Cl^- [Watanabe et al., 1999]. However, further investigations are needed to clarify the effects of impurities on grain growth rates.

References

Alley, R. B., A. J. Gow and D. A. Meese. 1995. Mapping c-axis fabrics to study physical processes in ice. *J. Glaciol.*, 41(137), 197-203.

Alley, R. B. and G. A. Woods, 1996. Impurity influence on normal grain growth in the GISP2 ice core, Greenland. *J. Glaciol.* 42(141), 255-260

Azuma, N. and 6 others. 1999. Textures and fabrics in the Dome F (Antarctica) ice core. *Ann. Glaciol.*, 29, in press.

Dome-F Deep Coring Group. 1998. Deep ice core drilling at Dome Fuji and glaciological studies in east Dronning Maud Land, Antarctica. *Ann. Glaciol.*, 27, 333-337.

Goodman, D. J., H.J. Frost and M.F. Ashby. 1977. Effect of impurities on the creep of ice Ih and its illustration by the construction of deformation maps. *IAHS.*, 118, 17-22.

Gow, A. J. and T. Williamson. 1976. Rheological implications of the internal structure and crystal fabrics of the West Antarctic ice sheet as revealed by deep core drilling at Byrd Station. *Geol. Soc. Am. Bull.*, 87(12), 1665-1667.

Gow, A. J and 6 others. 1997. Physical and structural properties of the Greenland Ice Sheet Project 2 ice cores: A review. *J. Geophys. Res.*, 102(C12), 26559-26575.

Herron, S. L. and C. C. Langway Jr. 1982. A comparison of ice fabrics and textures at Camp Century, Greenland and Byrd Station, Antarctica. *Ann. Glaciol.*, 3, 118-124.

Herron, S. L., C. C. Langway Jr. and K. Brugger. 1985. Ultrasonic velocities and crystalline anisotropy in the ice core from Dye 3, Greenland. *Greenland Ice Core: Geophysics, Geochemistry and the Environment*, edited by C. C. Langway Jr., H. Oeschger and W. Dansgaard. Geophys. Monogr. Ser., 33, AGU, Washington, DC, 49-56.

Koerner R. M. and D. A. Fisher. 1979. Discontinuous flow, ice texture, and dirt content in the basal layers of the Devon Island ice cap. *J. Glaciol.*, 23(89), 209-222.

Langway, C. C., Jr., H. Shoji and N. Azuma. 1988. Crystal size and orientation patterns in the Wisconsin-age ice from Dye 3, Greenland. *Ann. Glaciol.*, 10, 109-115.

Lipenkov, V. Y. and 3 others. 1989. Crystalline texture of the 2083-m ice core at Vostok Station, Antarctica. *J. Glaciol.*, 35(121), 392-398.

Shoji, H. and A. Higashi. 1978. Deformation mechanism map of ice. *J. Glaciol.*, 21(85), 419-427.

Thorsteinsson, T. 1996. Textures and fabrics in the GRIP ice core, in relation to climate history and ice deformation. *Berichte zur Polarforschung*, 205.

Thorsteinsson, T. and 4 others. 1995. Crystal size variations in Eemian-age ice from the GRIP ice core, central Greenland. *Earth Planet. Sci. Lett.*, 131(3-4), 381-394.

Thorsteinsson, T., J. Kipfstuhl and H. Miller. 1997. Textures and fabrics in the GRIP ice core. *J. Geophys. Res.*, 102(C12), 26583-26599.

Wang, Y. and N. Azuma. 1999. The development of an automatic ice fabric analyzer by image-analysis techniques. *Ann. Glaciol.*, 29, in press.

Watanabe, O. and 5 others. 1999. Studies on paleoclimate signal. Recorded in the ice core from Dome Fuji Station, East Queen Maud Land, Antarctica. *Ann. Glaciol.*, 29, in press.

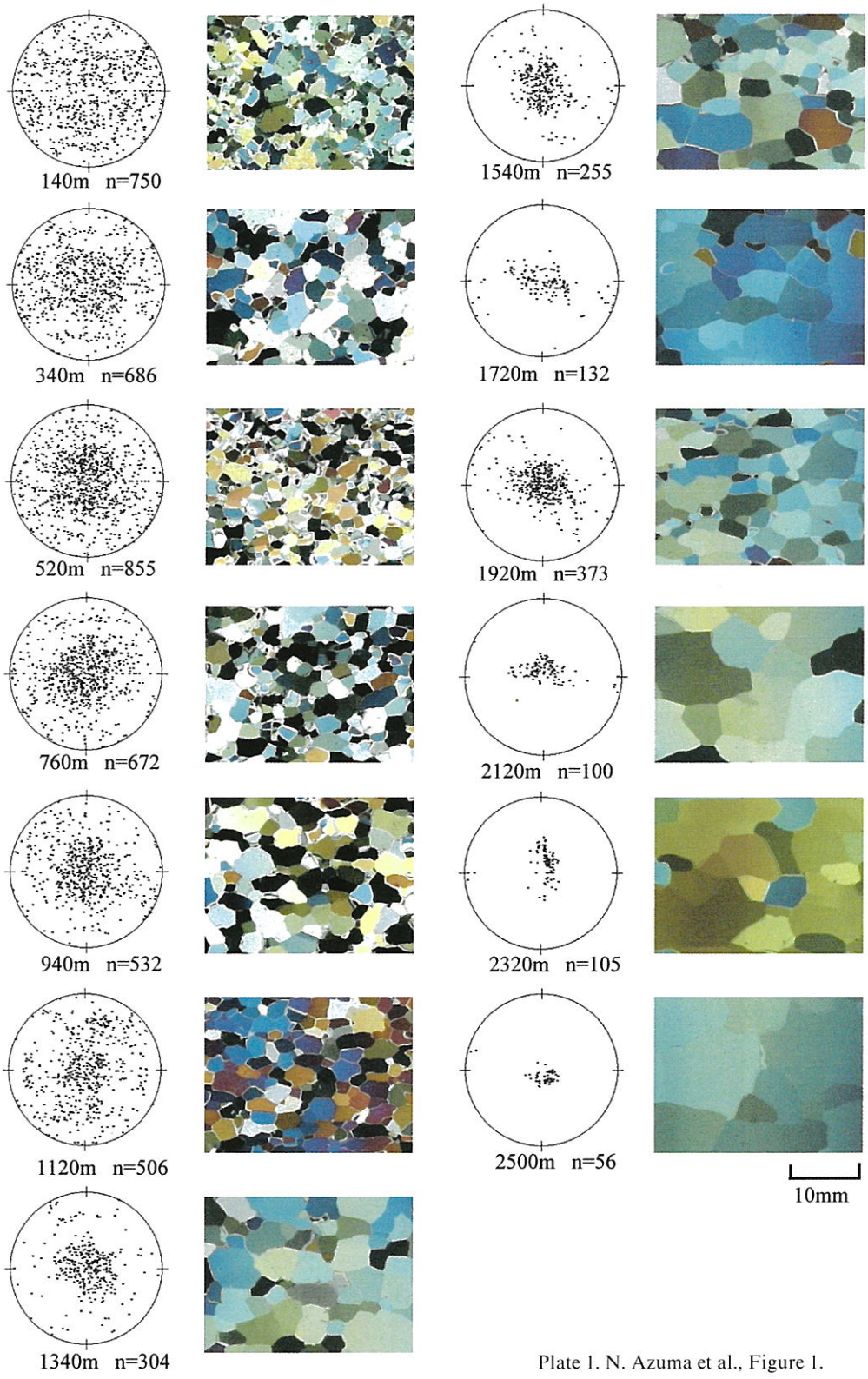

Plate 1. N. Azuma et al., Figure 1.

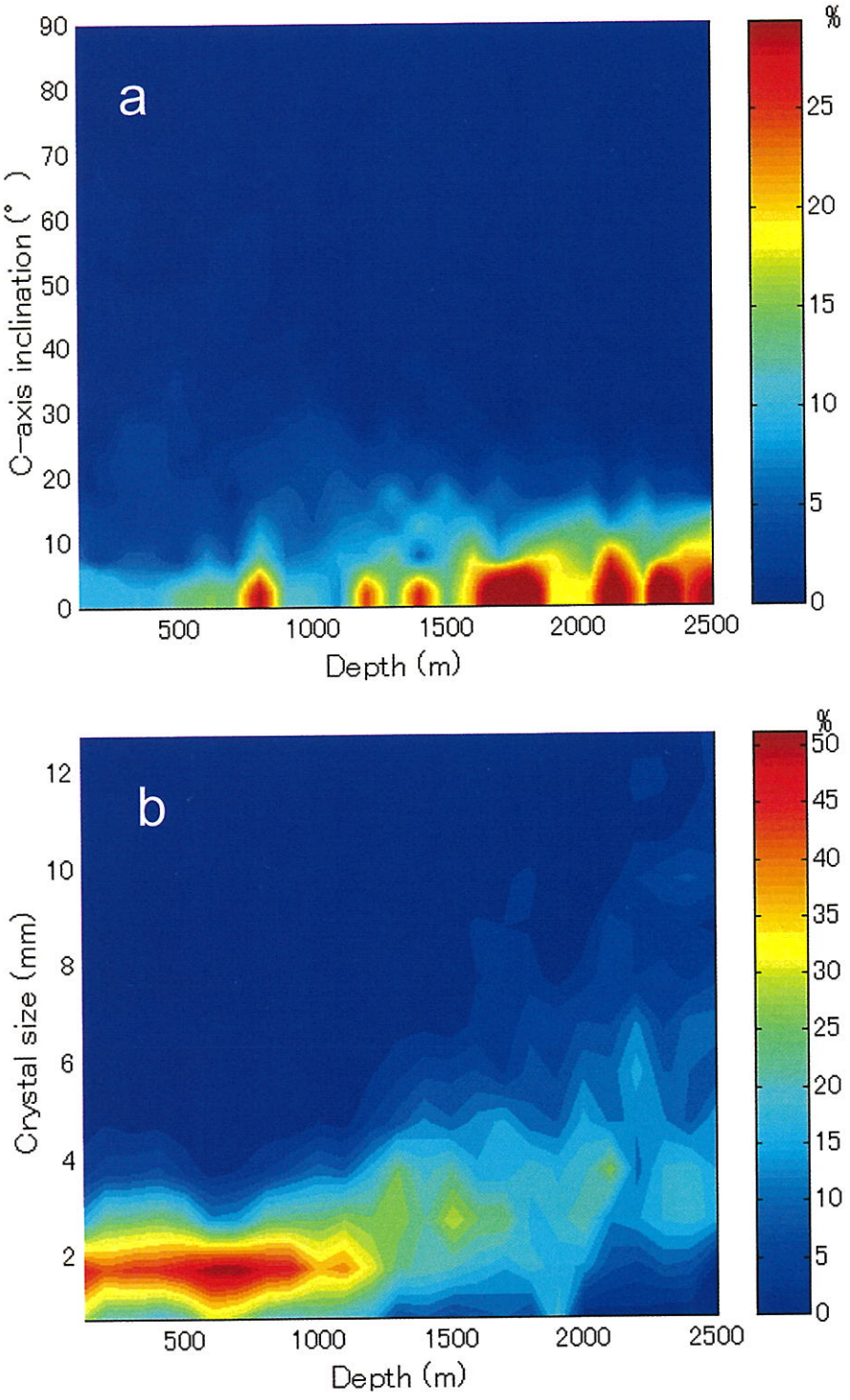

Plate 2. N. Azuma et al., Figure 2.

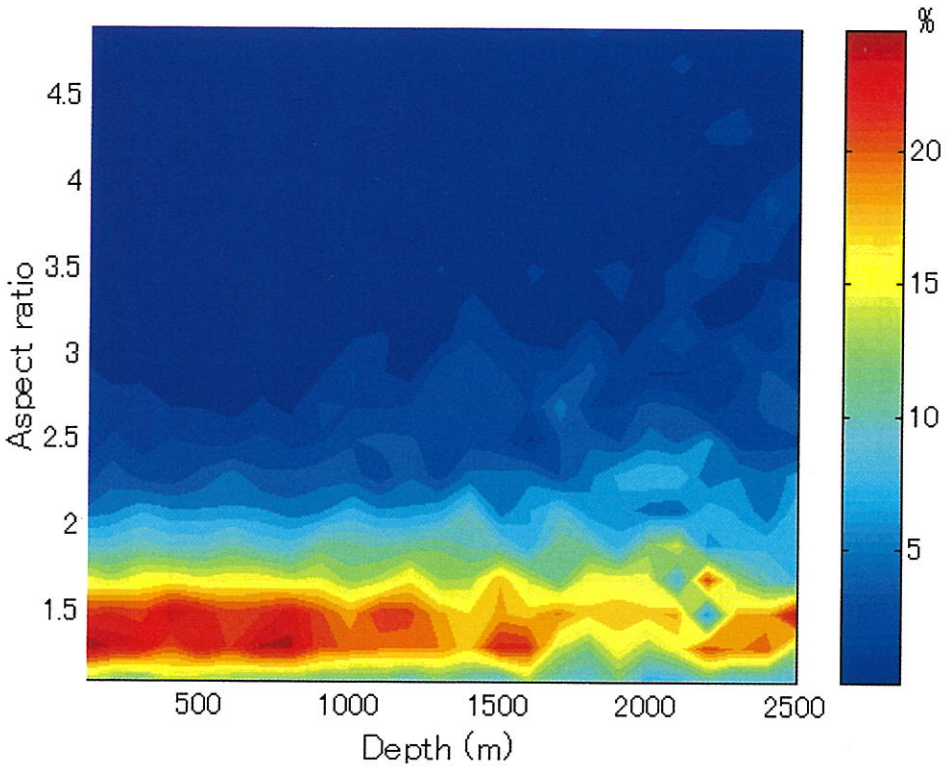

Plate 3. N. Azuma et al., Figure 6.

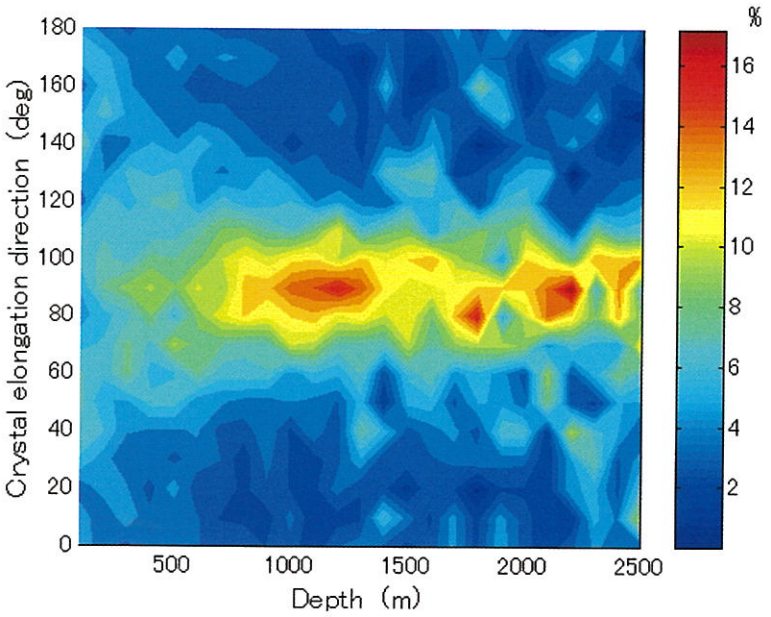

Plate 4. N. Azuma et al., Figure 8.

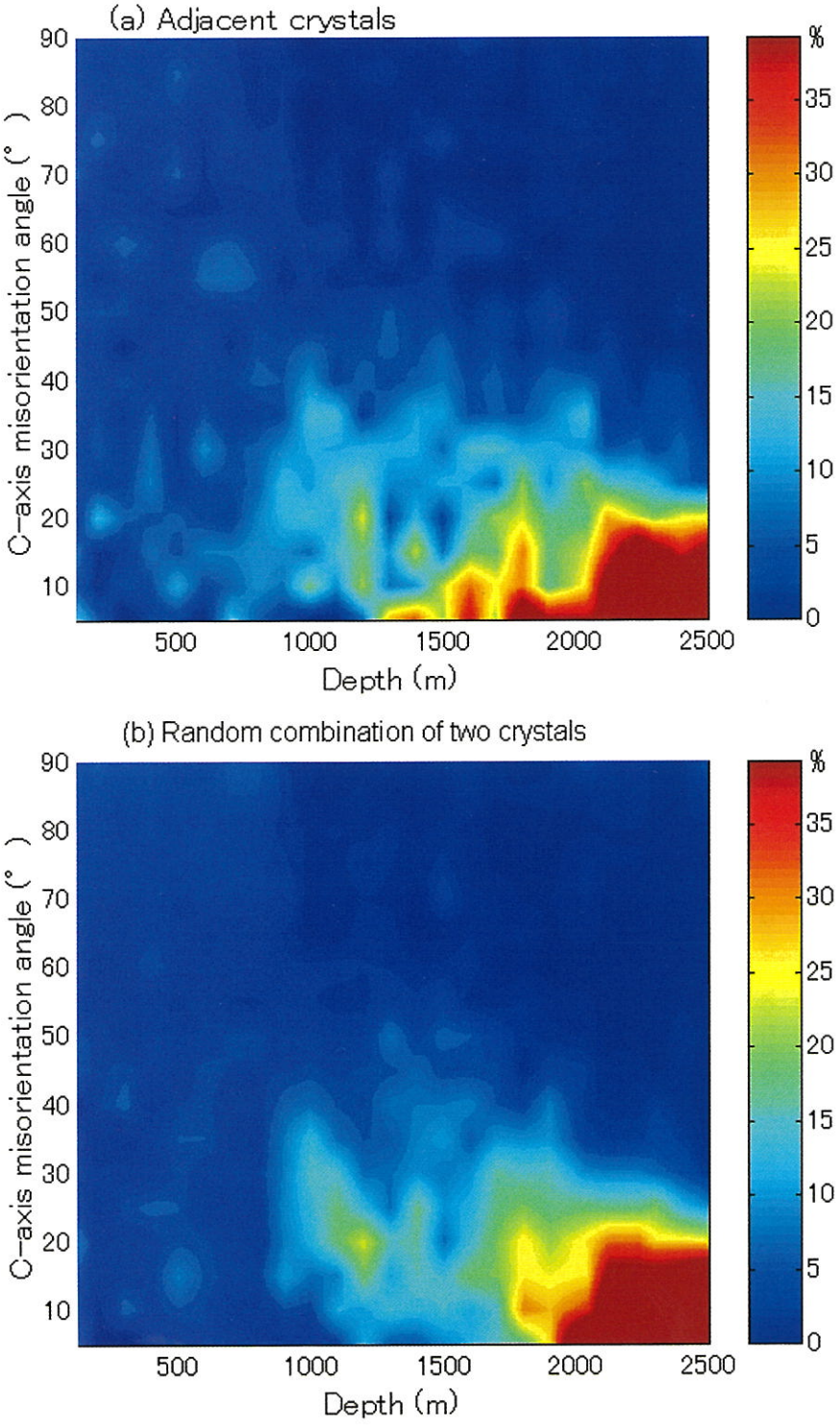

Plate 5. N. Azuma et al., Figure 10.

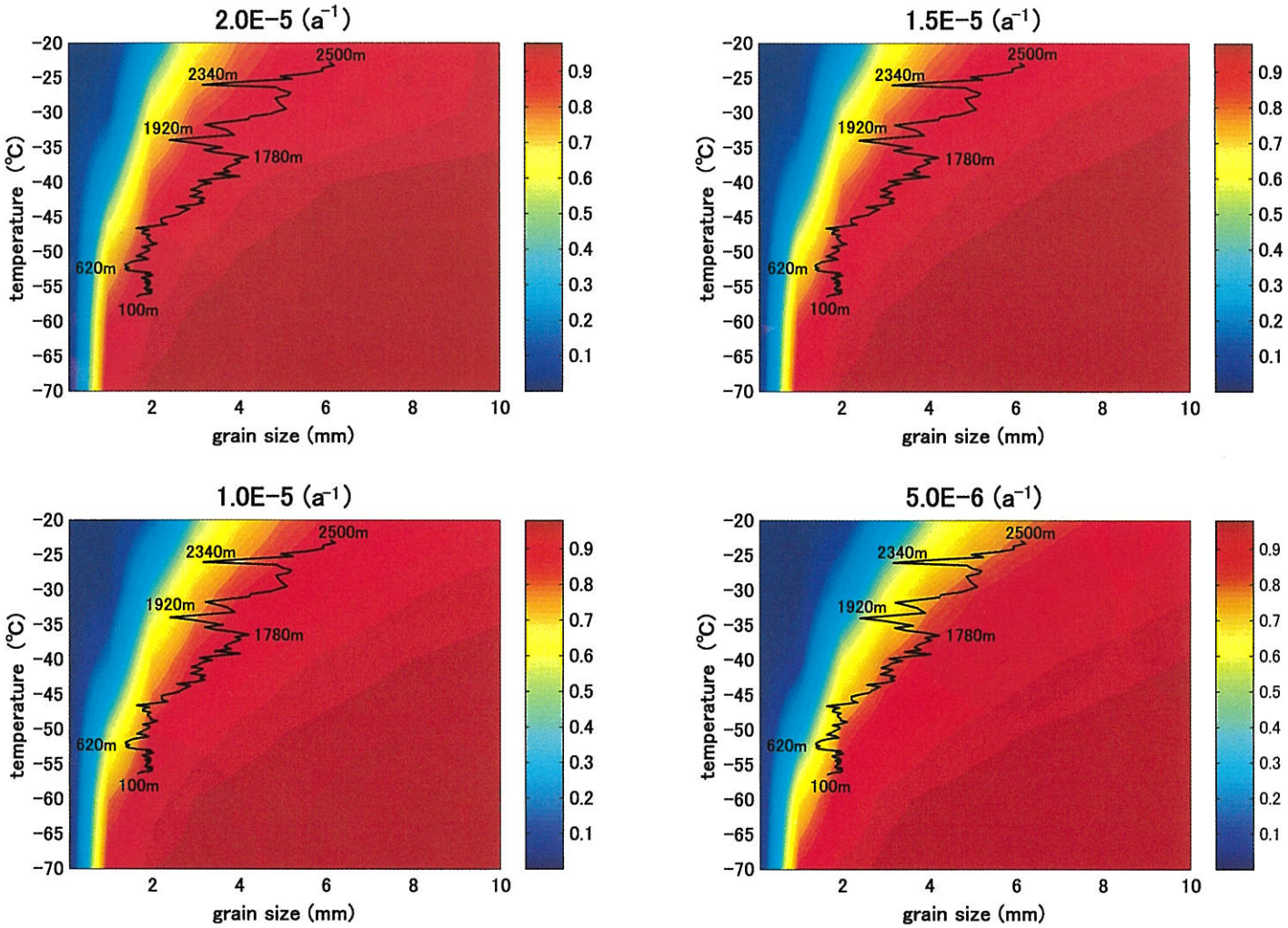

Plate 6. N. Azuma et al., Figure 13.